Nanoscale

# Novel Boron Nitride MXenes as Promising Energy Storage Materials



| | |
|---|---|
| Journal: | *Nanoscale* |
| Manuscript ID | NR-ART-05-2022-002807 |
| Article Type: | Paper |
| Date Submitted by the Author: | 20-May-2022 |
| Complete List of Authors: | Muraleedharan, Murali Gopal; Oak Ridge National Laboratory, Computational Sciences and Engineering Division<br>Kent, Paul; Oak Ridge National Laboratory, |
| | |

Nanoscale

ROYAL SOCIETY OF CHEMISTRY

ARTICLE TYPE

Cite this: DOI: 00.0000/xxxxxxxxxx

# Novel Boron Nitride MXenes as Promising Energy Storage Materials†

Murali Gopal Muraleedharan*[a] and Paul R. C. Kent[b]

Received Date
Accepted Date

DOI: 00.0000/xxxxxxxxxx

MXenes are promising materials for rechargeable metal ion batteries and supercapacitors due to their high energy storage capacities, high electrical and ionic conductivities, and ease of synthesis. In this study, we predict the structure and properties of hitherto unexplored Ti-boron nitride MXenes ($Ti_3BN$ and $Ti_3BNT_2$ where T=F, O, OH) using high-throughput density functional theory calculations. We identify multiple stable structures exhibiting high thermodynamic and mechanical stability with B and N atoms evenly dispersed in the lattice sites. The predicted properties of the BN MXenes show remarkable similarities to their carbide counterparts, including in their metallicity, elastic constants, and cation absorption properties. Significantly, these novel MXene compounds display high lithium storage capacities (>250 mAh/g), as well as suitability for non-lithium ion storage (Na, K, Ca, Mg), making them attractive candidates for both batteries and supercapacitors. This class of MXenes therefore merits further theoretical and experimental investigation.

## 1 Introduction

MXenes are two-dimensional (2D) materials synthesized by exfoliation or selective etching of layered ternary transition metal carbides known as MAX phases.[1,2] They have a chemical formula $M_{n+1}X_nT_x$, where M is an early transition metal, X is C or N, and T is a surface functional group like F, O, OH, etc.[3–6] They offer an attractive combination of high cation intercalation capacity[7], fast ionic transport[8], and high electrical conductivity[8,9]. Owing to this combination of properties and ease of synthesis, MXenes are promising for a wide range of applications including energy storage[10,11], water purification[12,13], catalysis[14–16], optoelectronics[17–19], biomedical[20–22], and wireless communication[23]. Since their discovery in 2011, many compositional and structural variations with distinct structural and electronic properties have been proposed and synthesized,[24,25] thereby broadening the MXene family to MBenes,[26–29] MXene alloys,[30] and i-MXenes[31,32].

The search for novel MXenes with desired properties, including long life and facile synthesis has occurred concurrently with advances in materials design strategies and the development of high-throughput computational frameworks.[33–36] One promising strategy to design new MXene compositions is by atomic transmutation, a method for substituting certain types of elements with their neighboring elements in the periodic table by keeping the total number of valence electrons unchanged.[37,38] By starting transmutation with a known stable material the likelihood of finding new stable materials is high. A perfect example for the success of this method is hexagonal boron nitride (h-BN), where 2 carbon atoms of graphene substituted by B and N respectively, resulting in a material with a substantial band gap (5.9 eV) and larger lattice constant than metallic graphene (2.504 Å vs. 2.458 Å).[39] h-BN also possesses high thermal conductivity and excellent tribological properties that render it as a lubricant and high-temperature ceramic material.[40]. Inspired by the success of h-BN, a similar isoelectronic B and N substitution of C atoms in MXenes is a promising yet underexplored route for *in silico* MXene design. The possibility of a successful synthesis is also suggested by the recent growth of MBenes,[29,41] including in single layers[42], indicating that boron can be incorporated into MXene-like structures, and success in growth of carbon-nitride MXenes, e.g.[43–45].

There have been very few studies on the potential properties of boron nitride MXenes and their potential applications.[46,47]. Wang *et al.*[46] explored the stability, structural and electronic properties of $Ti_3BN$ monolayer using density functional theory (DFT) calculations. By considering a Ti-N-Ti-B-Ti sequence for the monolayer, which in essence, has B and N in separate layers, a global energy minimum structure for $Ti_3BN$ monolayer was

[a] *Computational Sciences and Engineering Division, Oak Ridge National Laboratory, Oak Ridge, TN 37831; E-mail: muraleedharm@ornl.gov*
[b] *Computational Sciences and Engineering Division, Oak Ridge National Laboratory, Oak Ridge, TN 37831; E-mail: kentpr@ornl.gov*

searched by particle-swarm optimization (PSO). They report good dynamic and structural stability for the monolayer, and also find that $Ti_3BN$ is metallic whose band gap can be tuned via functionalization. However, they did not report mechanical properties or lithium storage capacities. A study on $Ti_2BN$ was also performed using DFT.[47]. However, the structure adopted for this study was not strictly a conventional MXene (space group P63/mmc). They reported an excellent stability of $Ti_2BN$ and its potential application as an anode in Li-ion electrochemical energy storage systems.

In spite of these efforts, a comprehensive search for the preferred ground state structure has not been performed. B and N atoms were considered in 2 different planes and the possibility of dispersed (alloy-like) B and N phases were not explored. Dispersed BN phases potentially open up a new avenue for compositional and structural tuning of properties of MXenes systems. Key unanswered questions for these phases therefore include:

- What are the most stable boron nitride structures: are B and N in separate planes or intermingled?
- How do the energetic, structural, mechanical, and electronic properties of these boron nitrides compare with conventional carbide MXene counterparts?
- What are the trends in their Li, Na, K, Mg and Ca absorption and their suitability as anode materials?

To answer these questions, we consider four different classes of base boron nitrides: bare non-functionalized ($Ti_3BN$) and functionalized by F ($Ti_3BNF_2$), O ($Ti_3BNO_2$), and OH ($Ti_3BN(OH)_2$). In each of these case, we use combinatorial substitution to populate the C sites with B and N sites yielding all possible alloy combinations in each base class. Then, we perform high throughput DFT on these compounds to calculate relevant properties. Stable candidates are then chosen and subjected to a comprehensive analysis of their structural, electronic, and lithium storage properties.

## 2 Computational Methods

$Ti_3X_2T_2$(X=C; T=F, O, OH) primitive cell structures with space group P63/mmc were obtained from the Computational 2D Materials Database (C2DB)[33,48]. Starting from these primitive cells, the boron nitride structures were generated using a combinatorial substitution of C at the X sites of $2 \times 2 \times 1$ $Ti_3X_2T_2$ supercells with 50% each of B and N atoms, yielding 9 unique structures of each base class consisting of B and N atoms dispersed at the different X sites. Figure 1 shows the 9 unique structures of $Ti_3BN(OH)_2$ within our chosen supercell. We have adopted an indexing scheme ranging from i00-i08, where each index represents a configuration with a unique arrangement of B and N atoms in the X-site. The other atoms, *viz.* Ti, O, and H positions are the same for all the configurations. Note that i04 and i08 have ordered B and N layers in two different planes whereas the others have B and N atoms randomly dispersed in X sites. In addition to these 36 structures, the four $Ti_3C_2T_2$ structures were also included in our calculations for comparison.

In the first stage involving prediction of stability, structure, energetics, mechanical, and electronic properties, DFT calculations

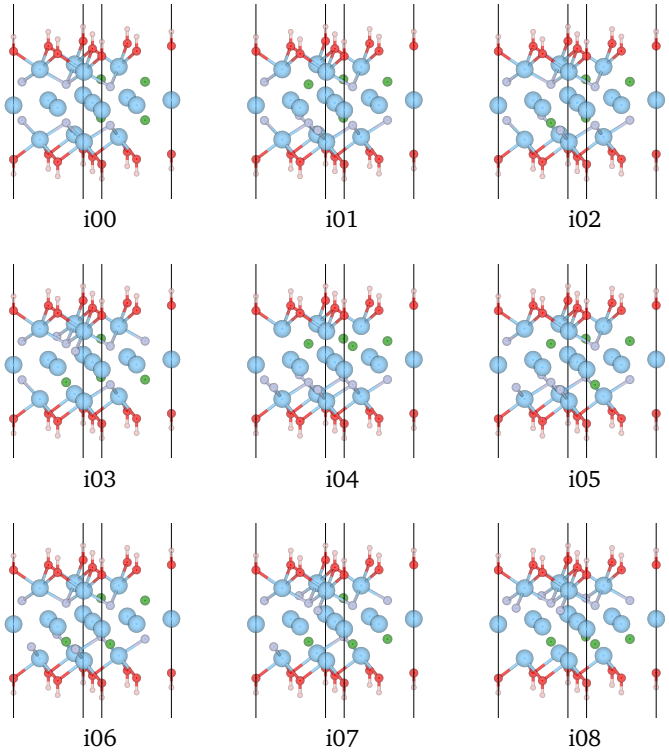


**Fig. 1** Unique structures (i00 to i08) of $Ti_3BN(OH)_2$ generated via combinatorial substitution of C atoms in 2x2x1 supercell of $Ti_3C_2(OH)_2$. Colors: oxygen (red), hydrogen (white), titanium (blue), boron (gray), nitrogen (green).

were performed using the projector augmented wave (PAW) code GPAW within the Perdew–Burke–Ernzerhof (PBE)[49] generalized gradient approximation (GGA) using plane wave (PW) basis sets and PAW potentials version 0.9.2.[50] We also used a more accurate Heyd-Scuseria-Ernzerhof (HSE06)[51,52] hybrid functionals to predict the electronic structure, to validate the PBE calculations. To ensure a streamlined and reproducible computational procedure of all the distinct structures, we have adopted a high-throughput DFT workflow that was originally developed to generate the C2DB.[33] The workflow consists of Atomic Simulation Recipes (ASR)[53], a library of convergence verified, numerically accurate python scripts based on GPAW, and managed using the atomic simulation environment (ASE)[54] to perform tasks in the workflow. Full details on the methods and parameters used for various steps can be found elsewhere.[33] These recipes have been rigorously tested for convergence in energy, forces, k-point density, PW cutoff, Fermi smearing, strains, and atomic displacements for phonon calculations, rendering a good agreement with available experimental results for a great many 2D materials including carbide MXenes.

In the second stage calculations involving the ion storage voltage, electron localization and charge density of candidate materials, PBE-GGA implemented in the Vienna *ab initio* Simulation Package (VASP) 6.1.1[55] was used. A 600 eV cutoff energy for the PW basis set and a $12 \times 12 \times 1$ k-space space sampling mesh was found to adequately converge the stress for cell shape relax-

ation. Lattice parameters and atomic positions were relaxed until the atomic forces were below 0.005 eV/Å. Structures with full ion coverage, i.e., Li, Na, K, Ca or Mg atoms on both sides of MXene sheet, on the X-site were used. We have used $2\times2\times1$ monolayers with two adsorbent atoms per formula unit placed directly above and below the C, B, or N atoms. This configuration has shown to be the most favorable site of Li atom intercalation[56,57].

# 3 Results

## 3.1 Screening materials based on stability criteria

### 3.1.1 Thermodynamic stability

We first identify out the most thermodynamically stable configurations among the different structures. For this, we first quantify thermodynamic stability by means of energy above convex hull (E-hull).[58] E-hull defines phases with energies below those for all possible mixtures of competing phases with the same compositions. For a material to be stable, its E-hull should be $\leq 0$. With positive E-hull, the material would eventually decompose to various constituent phases with lower formation energies. However, for a 2D material like MXene which is exfoliated from bulk MAX phases, we also need to account for the exfoliation energy. A stable 2D material could still have E-hull $\geq 0$ but to know the appropriate threshold, we need to benchmark computed E-hull values against experimentally synthesized stable structures.

Calculation of E-hull using DFT and isolated MXenes has limitations when compared to experiment including from uncertainty in the energies arising from the approximate exchange-correlation functional, exclusion of substrate interactions that can stabilize the monolayer, and kinetic barriers that separate the monolayer from other lower energy phases leaving the monolayer in a metastable state.[33] Hence, here we consider materials with E-hull $< 0.4$ eV/atom to be sufficiently stable, following the rationale in prior works on 2D materials.[33,48,59]

To determine E-hull, we have obtained the PBE formation energies of constituent molecules from the Open Quantum Materials Database (OQMD). Figure 2 (a)-(d) shows the calculated E-hull relative to the lowest energy structure in each category. The first step of stability screening involves identifying the lowest energy structure in each base class. As can be seen from Figure 2, the lowest energy structures of $Ti_3BN$ has an i02 configuration whereas that of the functionalized compounds have i00 configuration. However, the i02 configurations are next closest in energy, a maximum of 0.04 eV higher. These configurations (Fig. 1) differ by the relative placement of the B/N atoms in different plane: in i00 they are aligned in the out-of-MXene direction, while in i02 they are not. Also note the variation in energy ranges. The $Ti_3BN$ class shows the broadest range in values with the i04 and i08 configurations nearly 0.4 eV/atom higher than the i02 configuration. The i04 and i08 configurations are the structures that place in B and N atoms in separate planes. Structures with a more uniform distribution are lower in energy. With functionalization, the spread in energies decreases by an order of magnitude. $Ti_3BN(OH)_2$ has the narrowest spread of 0.053 eV/atom, followed by $Ti_3BNO_2$ (0.062 eV/atom) and $Ti_3BNF_2$ (0.095 eV/atom). Also note that, in all the four cases, i04 and i08 exhibit the highest E-hull values.

### 3.1.2 Phonons and dynamic stability

We continue screening candidates based on their phonon (dynamic) stability. Under equilibrium, a crystal is dynamically stable if its energy increases as a function of any combinations of atomic displacements.[60] This means that all phonons have real and positive frequencies. In the case of a negative or imaginary phonon frequency, the system is deemed to be dynamically unstable, which means that atomic displacements reduce the energy in the vicinity of the equilibrium atomic positions.

To assess the dynamic stability of the four high phase stability compounds, we determine the phonon band structure in the high symmetry directions within the first Brillouin zone as shown in Figure 3. Figure 3 (a), (b), and (d) represent all positive phonon modes suggesting that $Ti_3BN$, $Ti_3BNF_2$, and $Ti_3BN(OH)_2$ are dynamically stable. From Figure 3 (c), $Ti_3BNO_2$ has two noticeable imaginary acoustic phonon branches indicating a dynamic instability. Considering the possibility of this apparent imaginary mode to be a numerical artifact, we recalculated the phonon band structure following a more stringent structural relaxation (from 0.01 eV/Åto 0.0001 eV/Å) and subjected to a denser K-points sampling (from 6.0/Å$^{-1}$ to 12.0/Å$^{-1}$), and confirmed that the instability is in fact, physical. Therefore, it is highly unlikely that this material can be directly synthesized in its freestanding form.

Examination of the phonon band structures for $Ti_3BN$, $Ti_3BNF_2$, $Ti_3BN(OH)_2$ shows slight imaginary frequency modes near the gamma point, which we consider convergence artifacts arising from limited supercell size.[60,61] Phonon band structure calculations are computationally expensive and the cost increases cubically with the number of atoms. Whereas a thorough phonon stability analysis would require a rigorous supercell convergence study, since our focus is primarily on a high-level screening, we have used the standard supercell size suggested by the workflow. Based on dynamic stability screening, we have narrowed down to three stable BN analogues, whose mechanical stability needs to be analyzed.

### 3.1.3 Elastic constants and mechanical stability

We further performed a mechanical stability analysis of the three MXenes based on the stability criteria following Mouhat and Coudert.[62] This states that the necessary and sufficient conditions for a 2D hexagonal crystal lattice to be mechanically stable, are, $C_{11}.C_{22} - {C_{12}}^2 > 0$ and $C_{66} > 0$, where $C_{66} = (C_{11} - C_{12})/2$, which is a generalized version of Born stability conditions.[62] The elastic constants of a material are defined by Hooke's law:

$$\sigma_{ij} = C_{ijkl}\varepsilon_{kl} \tag{1}$$

where $\sigma_{ij}$, $\varepsilon_{kl}$, and $C_{ijkl}$ are the stress, strain, and elastic tensors respectively. For a 2D material, this relationship between planar stress and strain gives rise to the following matrix equation:

$$\begin{bmatrix} \sigma_{xx} \\ \sigma_{yy} \end{bmatrix} = \begin{bmatrix} C_{11} & C_{12} \\ C_{12} & C_{22} \end{bmatrix} \begin{bmatrix} \varepsilon_{xx} \\ \varepsilon_{yy} \end{bmatrix} \tag{2}$$

The elastic stiffness constants $C_{11}$, $C_{22}$, and $C_{12}$ calculated using

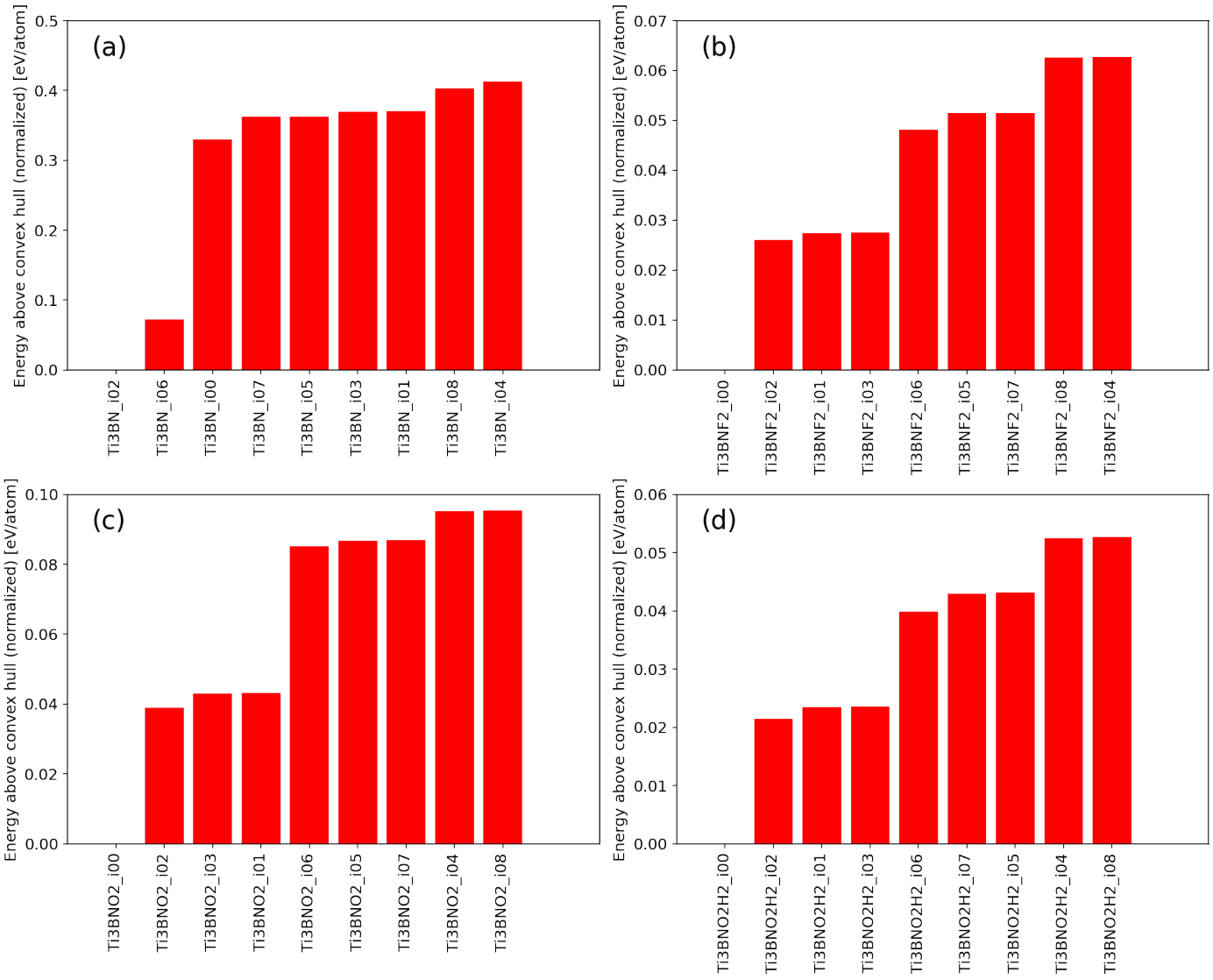


**Fig. 2** Energy above convex hull relative to the lowest energy structure. (a) $Ti_3BN$, (b) $Ti_3BNF_2$, (c) $Ti_3BNO_2$, and (d) $Ti_3BN(OH)_2$.

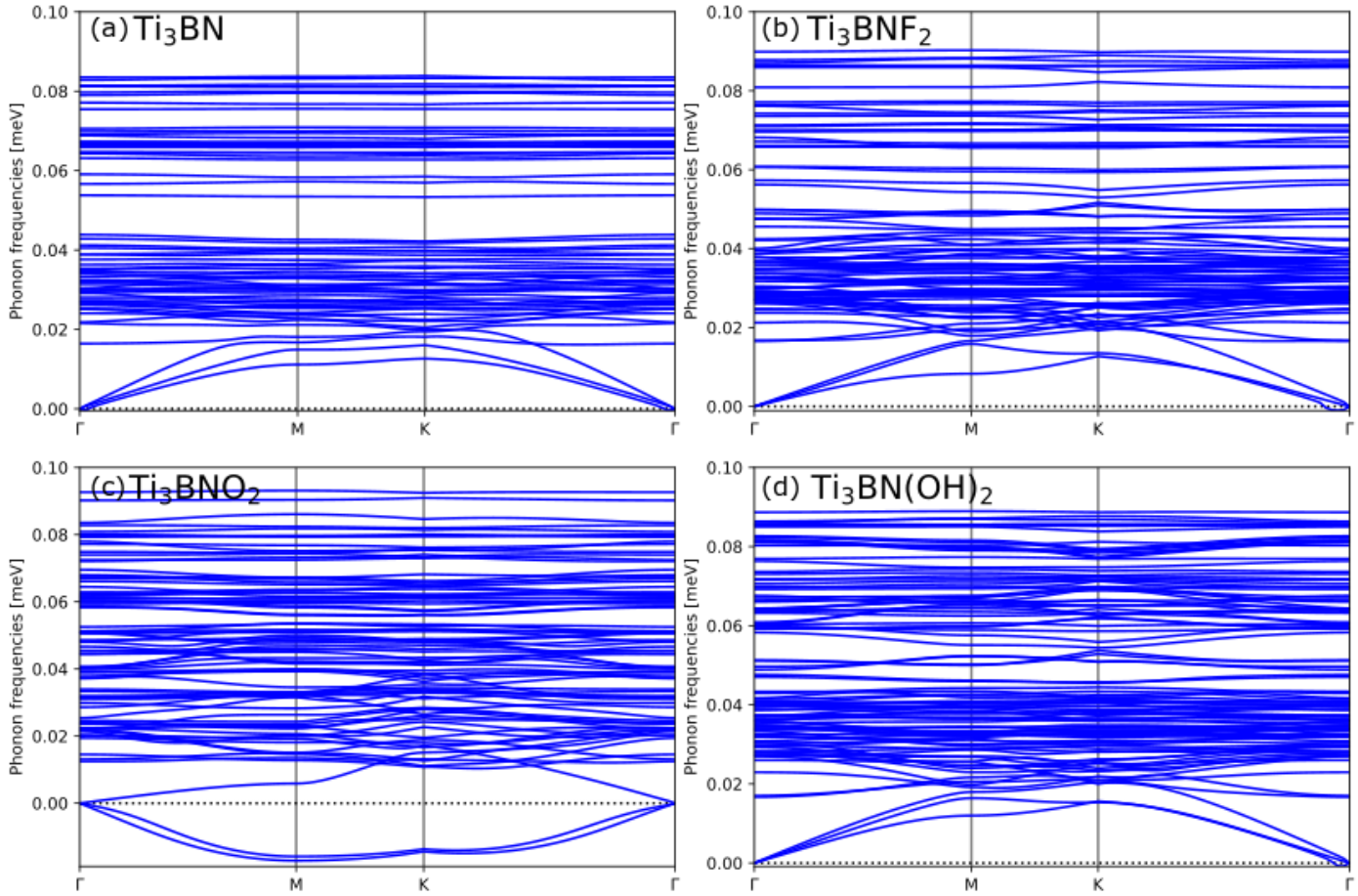


**Fig. 3** Phonon dispersion relations of the highest thermodynamic stability structures. (a) $Ti_3BN$, (b) $Ti_3BNF_2$, (c) $Ti_3BNO_2$, and (d) $Ti_3BN(OH)_2$.

| Material | $C_{11}$ (N/m) | $C_{12}$ (N/m) | $C_{22}$ (N/m) | $Y_1$ (N/m) | $Y_2$ (N/m) |
|---|---|---|---|---|---|
| $Ti_3C_2$ | 253.07 | 48.51 | 252.84 | 243.54 | 243.76 |
| $Ti_3C_2F_2$ | 361.79 | 108.73 | 361.02 | 328.34 | 329.04 |
| $Ti_3C_2(OH)_2$ | 191.67 | 9.31 | 199.19 | 198.73 | 191.23 |
| $Ti_3BN$ | 187.18 | 33.97 | 190.66 | 184.49 | 181.13 |
| $Ti_3BNF_2$ | 269.05 | 64.97 | 265.57 | 249.88 | 253.15 |
| $Ti_3BN(OH)_2$ | 273.45 | 58.19 | 273.81 | 261.42 | 261.08 |

**Table 1** Elastic constants of boron-nitride and carbide MXenes.

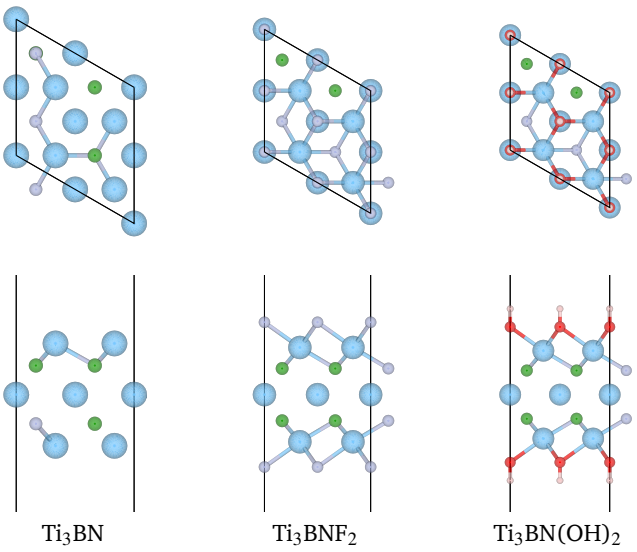


**Fig. 4** Top and side views of stable predicted structures. The bonds drawn are a guide to the eye only. Colors: oxygen (red), hydrogen (white), titanium (blue), boron (gray), nitrogen (green).

a central difference approximation to the derivative of the stress tensor. Here, in effect, the material is strained by $\pm 1\%$ along one of the axes x or y, and the stress tensor is calculated. Likewise, the Young's modulii $Y_n$, where n=1,2 is calculated by the equation[63]:

$$Y_n = \frac{C_{11}.C_{22} - {C_{12}}^2}{C_{nn}} \quad (3)$$

Table 1 shows the elastic constants of carbide MXenes and BN analogues. The elastic constants of carbide MXenes compare well with the values reported in the literature,[64] thereby validating the current calculations. In general, the elastic constants are of the same order for carbides and boron nitrides, suggesting that these compounds have comparable mechanical strength. While $Ti_3BN$ and $Ti_3BNF_2$ has slightly lower mechanical strength, the $Ti_3BN(OH)_2$ has a higher strength than its carbide counterpart. Also note that all the three candidate materials satisfy the generalized Born mechanical stability criteria.

It is important to note that all these configurations consist of B and N atoms evenly dispersed, as opposed to what is reported in prior studies[46,47] that the energetically favorable structure is one with B and N atoms in different planes. Our phase stability calculations show that these structures, i04 and i08 respectively, have the highest energy, rendering them the least phase stable among the different configurations. What is not clear from the stability analysis is long term environmental stability. Prior studies based on electrical conductivity have shown that colloidal $Ti_3C_2T_x$ MXene solutions in water almost completely oxidizes within a few days when exposed to air.[65] However, Ar-dried $Ti_3C_2T_x$ flakes are more stable hence reiterating the importance of water in degrading MXene structures. While the long-term stability of BN MXenes are beyond the scope of the current study, considering that they are isoelectronic with carbide MXenes with comparable formation energy and E-hull values, we believe that their long-term stability would also be similar to that of the carbide counterparts. In summary, based on a thorough stability screening, we have identified three stable compounds as shown in Figure 4, which are subjected to property analysis.

### 3.2 Energetic and Structural Properties

The E-hull and formation energies of stable compounds are given in Table 2. The BN analogues have higher formation energies compared to the carbides. By contrasting their E-hull, in general, they have comparable stability values. $Ti_3BN$ has a lower E-hull than $Ti_3C_2$ indicating higher thermodynamic stability whereas the $Ti_3BNT_2$ have a marginally lower thermodynamic stability than their carbide counterparts.

We then proceed to analyze the ground state structural properties, namely lattice constant (a), monolayer thickness (L), and bond lengths (d) between Ti and X ($d_{Ti-C}$, $d_{Ti-B}$, and $d_{Ti-N}$), and between Ti and T ($d_{Ti-T}$). These are also given in Table 2. While the lattice constant is slightly larger for the BN analogues, the monolayer thickness is lower, except for bare $Ti_3BN$. Both Ti-B and Ti-N bond lengths are shorter than Ti-C bond length. Ti-C bonds have shown to be shorter than Ti-N bonds[66] in MXenes correlating with their atomic radii. It is also important to note that the Ti-T bond length decreases with BN substitution suggesting an enhanced bonding between Ti and the functional groups.

### 3.3 Electronic Properties

#### 3.3.1 PBE calculations

We then computed the electronic properties of these materials. All the materials have zero band gap in PBE DFT, and are hence, metallic. While our computational protocol allows for spin-polarization and potentially magnetic ground states, all the stable materials are predicted to be non-magnetic in PBE DFT. We also calculated the orbital projected band structure (PBS) to analyze the atomic orbital contributions to the wave functions for different bands as a function of k-points. To complement PBS, the projected density of states (PDOS) is also calculated, which resolves the atomic orbital contributions to the total density of states (DOS).

Figure 5 shows the PBS-PDOS of carbides and their boron nitride counterparts. The relative orbital contribution to the given Bloch state is indicated by a pie chart symbol on the bands. For all the six compounds, we observe that, Ti-d has the highest contribution to the DOS, which contribute to the high density of electronic states around the Fermi level. This in turn enhances the electrical conductivity of the monolayers. Also note that, below Fermi energy, Ti-p and Ti-d contributions are roughly equal but above $E_f$, the Ti-p contribution reduces. Comparing $Ti_3C_2$ and

**Table 2** Thermodynamic and structural properties of boron nitride and carbide MXenes.

| Material | E-hull (eV/atom) | Formation energy (eV) | a (Å) | L (Å) | $d_{Ti-C}$ (Å) | $d_{Ti-B}$ (Å) | $d_{Ti-N}$ (Å) | $d_{Ti-T}$ (Å) |
|---|---|---|---|---|---|---|---|---|
| $Ti_3C_2$ | 0.351 | -0.392 | 3.098 | 4.66 | 2.05 | - | - | - |
| $Ti_3C_2F_2$ | -0.067 | -0.932 | 3.037 | 7.23 | 2.20 | - | - | 2.17 |
| $Ti_3C_2(OH)_2$ | 0.115 | -1.302 | 2.993 | 9.22 | 2.20 | - | - | 2.19 |
| $Ti_3BN$ | 0.199 | -0.932 | 3.139 | 4.69 | - | 2.27 | 2.21 | - |
| $Ti_3BNF_2$ | 0.054 | -2.042 | 3.105 | 7.07 | - | 2.19 | 2.13 | 2.15 |
| $Ti_3BN(OH)_2$ | 0.198 | -1.441 | 3.120 | 9.02 | - | 2.19 | 2.18 | 2.17 |

$Ti_3BN$, the bands feature differences in their trends. For $Ti_3C_2$, we can identify three sets of sub-bands. The lowest energy (below -2 eV) sub-bands correspond to states mostly contributed by C-p, Ti-p and Ti-d orbitals roughly in equal proportion. In the mid-range (-2 to 0 eV), Ti-s contribution reduces and above $E_f$, Ti-d is the sole contributor. In the $Ti_3BN$, also we can identify roughly a similar distribution of bands but, the transition between low-energy sub-bands are rather gradual. At lower energies, B-p, Ti-p, and Ti-d are major contributors whereas as the contributions from N-p is minimal. At higher energy, similar to $Ti_3BN$, Ti-d is the predominant contributor. Since $Ti_3C_2$ was predicted to be ferromagnetic, we obtained spin-polarized PDOS whereas $Ti_3BN$ is non-magnetic, hence non-spin-polarized PDOS are presented in Figure 5. We also find similar trends in the functionalized MXenes.

#### 3.3.2 HSE06 calculations

While all the materials are predicted to be metallic in PBE DFT, we note that the predicted density of states near the Fermi energy is relatively low in the terminated boron nitrides. Given that PBE will generally underestimate band gaps, the possibility of a gap opening cannot be ruled out, either in experiment or in more accurate but computationally expensive calculations using HSE06 functional. We performed HSE DFT calculations on all the chosen compounds to obtain the electronic band structure. Figure 6 compares the PBE and HSE level band structures of the different compounds. As can be seen from the figure, there is a slight shift in the energy levels. However, for all the compounds, the band gap was still calculated to be zero, reiterating the fact that all the MXenes are in fact metallic in nature, and thereby validating the PBE predictions.

#### 3.3.3 Valence Electron Localization Function

To further analyze the electronic properties, we obtained the valence electron localization functions (ELF). 2D contour plots of normalized ELF along the (110) direction are shown obtained as shown in Figure 7(a)-(f). Here, 0.0 indicates no electrons, 0.5 indicates delocalized, and 1.0 indicates localized electron cloud. The region around Ti atoms has ELF value of 0.0 indicating the electron deficiency. Likewise, the regions in the vicinity of C atoms have electron localization surrounded by a region of delocalized electrons. A similar observation can be made for N atoms. However, for B atoms, there are regions of strong electron localizations surrounded by a background region of delocalized electron clouds suggesting B-B bond formation. Hence, for $Ti_3C_2$ and $Ti_3BN$, formation C-C and B-B bonds can be inferred from the respective ELF's. Also note in the region next to the monolayer surface, a region of strong electron localization is observed. For $Ti_3C_2$, a normalized ELF value of 0.65-0.7 is seen while in the case of $Ti_3BN$, this is more intense with a value of 0.95. This strong electron localization has been reported in the past for $Ti_4C_3$ and $Ti_4N_3$ MXenes[67] and may be attributed to the lone pair electrons of surface Ti atoms, which enhance the electronic conductivity of the MXene layers.

### 3.4 Ion storage capacities

Finally, we analyze the Li, Na, K, Ca, and Mg atom storage capacities of boron nitride and carbide MXenes. For this, we calculate the gravimetric ion storage capacity and voltage. Gravimetric ion storage capacity and open circuit voltage can be calculated following Ceder *et al.*[68]:

$$Q = \frac{nF}{M_f}, \tag{4}$$

where n is the number of electrons transferred per formula unit (in this case 2 for $Li^+$, $Na^+$, and $K^+$; 4 for $Ca^2+$ and $Mg^2+$), F is the Faraday constant, and $M_f$ is the mass of the formula unit. The open circuit voltage, V for Li adsorption can be estimated as:

$$V = \frac{-[E(Ti_3X_2T_2Li_2) - E(Ti_3X_2T_2) - 2\mu(Li)]}{2}, \tag{5}$$

where $E(Ti_3XT_2)$ is the total energy of the MXene compound, $E(Ti_3XT_2Li_2)$ is the total energy of the MXene after intercalation of two Li atoms per formula unit, and $\mu$ (Li) is the chemical potential of the Li.

The calculated gravimetric capacity and voltage are given in Table 3, which show excellent agreement with the published values[57]. The boron nitrides differ in capacity from the carbides by less than 2 mAh/g for monovalent ions and less than 4 mAh/g for bivalent ions. $Ti_3C_2$ has a higher voltage followed by $Ti_3F_2$ and by $Ti_3(OH)_2$. $Ti_3(OH)_2$ shows a negative voltage indicating that the reaction is unfavorable. Overall the BN analogues offer very similar gravimetric capacity as carbides owing to the same molecular mass, however the voltages are 0.1-0.2 V lower than carbide counterparts. When comparing the Li ion storage properties, boron nitride analogues have similar high gravimetric capacity to the carbides. For Na, K, Ca and Mg ion storage, this trend is continued. The BN MXenes, including $Ti_3BN(OH)_2$, show favorable adsorption, high capacities, and at slightly to significantly lower voltages to the carbides.

We also studied the charge transfer upon surface atom adsorption by considering lithiation as an example. For this, the charge density difference between lithiated and unlithiated MXenes were calculated, keeping the structures fixed at those of the lithiated case, as shown in Figure 8. We observe a significant

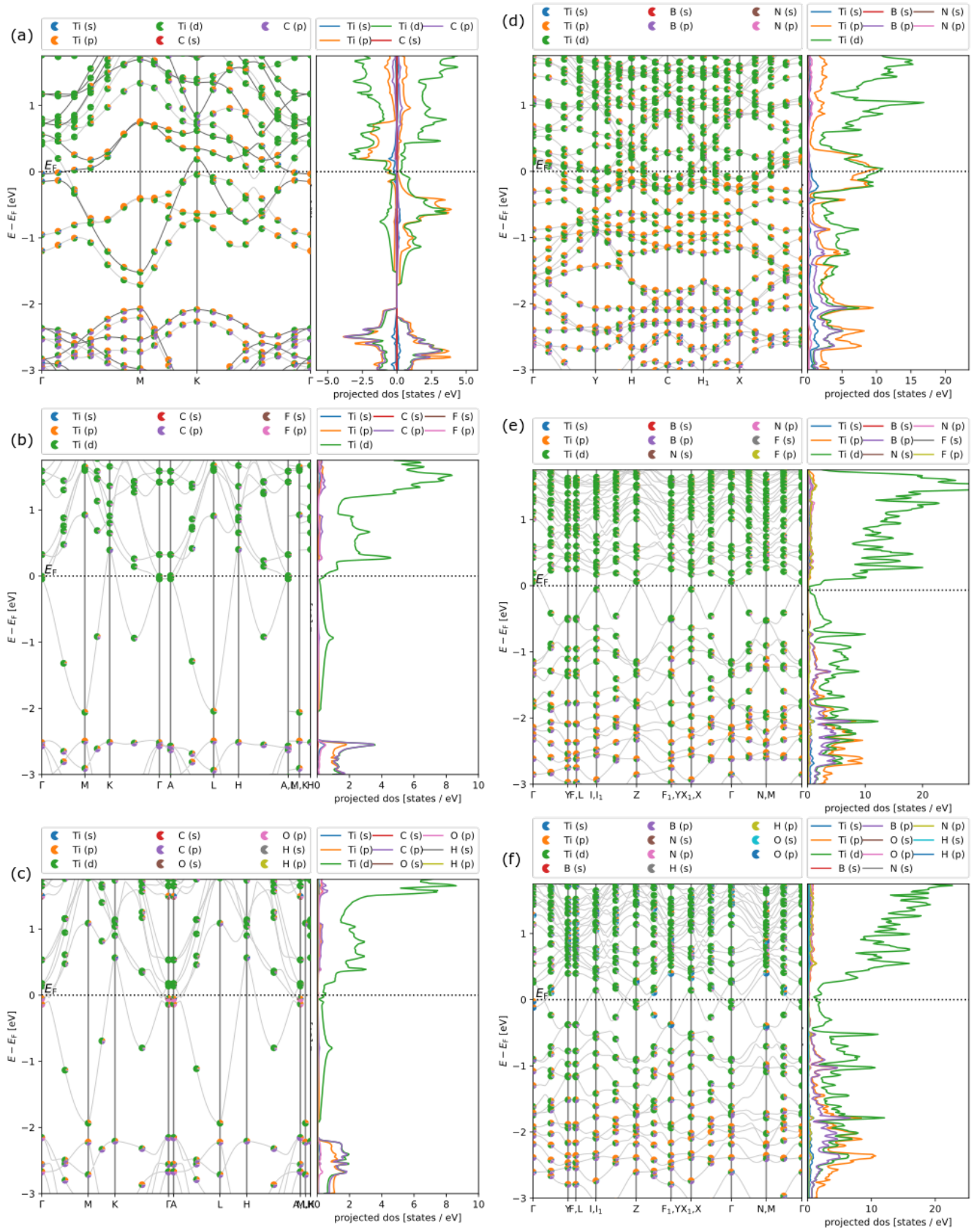


**Fig. 5** Projected band structure and PDOS of structures with high thermodynamic stability. (a) $Ti_3C_2$, (b) $Ti_3C_2F_2$, and (c) $Ti_3C_2(OH)_2$, (d) $Ti_3BN$, (e) $Ti_3BNF_2$, and (f) $Ti_3BN(OH)_2$.

| Material | Q (mAh/g) | | Open Circuit Voltage (V) | | | | |
|---|---|---|---|---|---|---|---|
| | Li/Na/K | Mg/Ca | Li | Na | K | Ca | Mg |
| $Ti_3C_2$ | 319.78 | 639.56 | 0.677 | -0.215 | 0.694 | -0.581 | 0.208 |
| $Ti_3C_2F_2$ | 260.69 | 521.37 | 0.339 | 2.197 | 4.039 | 2.675 | 3.153 |
| $Ti_3C_2(OH)_2$ | 265.84 | 537.04 | -0.583 | 0.441 | 1.138 | 0.308 | 1.328 |
| $Ti_3BN$ | 318.28 | 636.55 | 0.511 | -0.284 | 0.047 | -0.623 | 0.043 |
| $Ti_3BNF_2$ | 259.69 | 519.37 | 0.022 | -0.042 | 0.111 | 0.518 | -0.065 |
| $Ti_3BN(OH)_2$ | 264.79 | 578.17 | -0.709 | 0.003 | 0.295 | 0.311 | 0.586 |

**Table 3** Ion storage capacity and voltage of conventional MXenes and boron nitrides

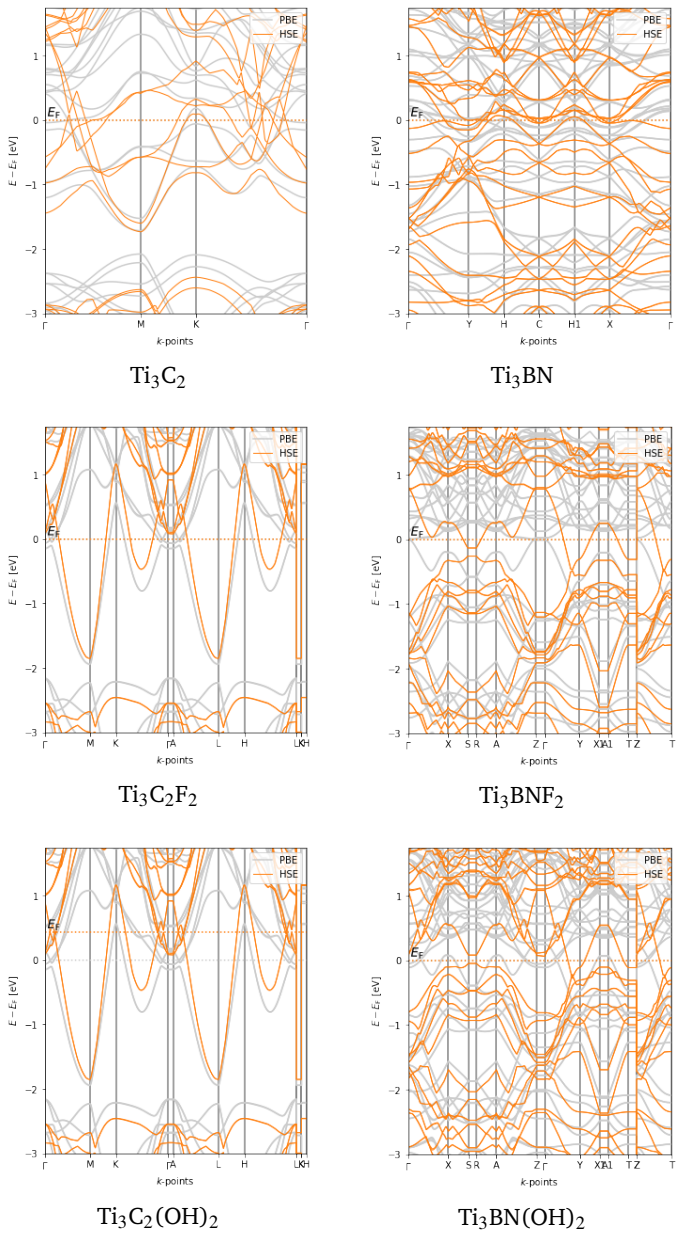


**Fig. 6** Comparison HSE06 and PBE level electronic band structures of $Ti_3C_2T_2$ and $Ti_3BNT_2$ MXenes

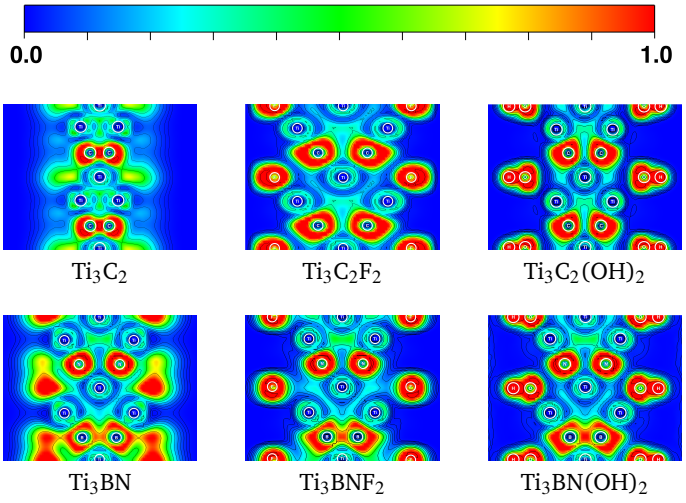


**Fig. 7** Valence electron localization function plotted along the (110) direction to include all the atoms of the primitive cell in a single plane

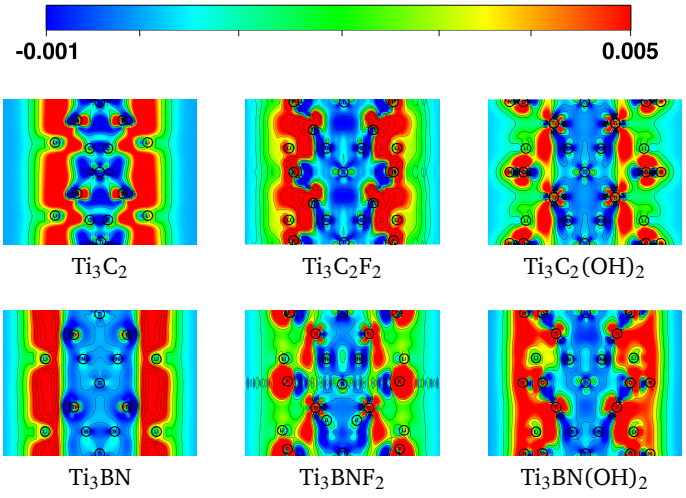


**Fig. 8** Charge density differences on lithiation plotted along the (110) direction to include all the atoms of the primitive cell in a single plane

charge transfer (electron depletion) from the Li to the MXene surfaces. For $Ti_3C_2$, the positive charge cloud penetrates closer to the carbon atoms than boron and nitrogen atoms, suggesting a stronger bond, and also explaining the higher absorption voltage. While the plots for bare $Ti_3C_2$ and $Ti_3BN$ are similar, the pattern of charge transfer with functional groups is visibly different. In the presence of functional groups, the positive charge cloud reduces in size indicating a weaker bond, which is also reflected in the corresponding voltage. However, in the case of $(OH)_2$ functionalization, we see more delocalization in the case of $Ti_3BN(OH)_2$ compared with $Ti_3C_2(OH)_2$, suggesting that the trend in voltage cannot be described fully by the charge density difference.

### 3.5 Pathways for experimental synthesis

The stable structures identified in the study are expected to be synthesizable using variations of the standard etching process that starts with the parent MAX phase, as in Ref. [8,69], or any of the subsequent refinements. A bottom up synthesis approach based on, e.g. chemical vapor deposition [70,71], may also be successful and would bypassing the requirements for the MAX phase and the chemical etching step.

## 4 Conclusions

We have identified stable boron nitride analogues to carbide MXenes ($Ti_3C_2T_2$) by means of reproducible high-throughput DFT workflows. We have identified three stable materials: $Ti_3BN$, $Ti_3BNF_2$, and $Ti_3BN(OH)_2$ with B and N atoms evenly dispersed at the X sites. For all the cases, configurations with even dispersed B and N atoms were found to be more thermodynamically favorable, as opposed to the configurations used in prior studies that have only explored B and N atoms confined to different planes. Moreover, structures with B and N atoms in different planes have the highest relative energy, rendering them the least phase stable among the different configurations. Both boron nitride and carbide MXenes were found to be metallic, with zero band gap. When comparing the Li ion storage properties, boron nitride analogues have similar high gravimetric capacity to the carbides. However, for K, Ca, and Mg ion storage, in many cases the BN MXenes have properties superior to the carbides, suggesting potential use for non-Li battery application. We therefore encourage experimental synthesis and characterization of these materials as well as additional theoretical work. Based on our results, we also consider it highly likely that many other, non-Ti MXenes with similar substitutions will be realizable.

## 5 Data Availability

For full reproducibility of the data and analysis presented here, complete datasets capturing the full computational workflows will be made available on publication. This includes the structures, charge densities, calculated total energies as well as complete details of each density functional calculation. A link to a public DOI will be placed here in the manuscript proof.

## 6 Acknowledgments

This research is sponsored by the Fluid Interface Reactions, Structures, and Transport (FIRST) Center, an Energy Frontier Research Center funded by the U.S. Department of Energy (DOE), Office of Science, Office of Basic Energy Sciences. This research used resources of the Compute and Data Environment for Science (CADES) at the Oak Ridge National Laboratory, which is supported by the Office of Science of the U.S. Department of Energy under Contract No. DE-AC05-00OR22725. This research used resources of the National Energy Research Scientific Computing Center, a DOE Office of Science User Facility supported by the Office of Science of the U.S. Department of Energy under contract no. DE-AC02-05CH11231.

## References

1 M. Naguib, M. Kurtoglu, V. Presser, J. Lu, J. Niu, M. Heon, L. Hultman, Y. Gogotsi and M. W. Barsoum, *Advanced Materials*, 2011, **23**, 4248–4253.

2 M. Alhabeb, K. Maleski, B. Anasori, P. Lelyukh, L. Clark, S. Sin and Y. Gogotsi, *Chemistry of Materials*, 2017, **29**, 7633–7644.

3 M. Khazaei, A. Ranjbar, M. Arai, T. Sasaki and S. Yunoki, *Journal of Materials Chemistry C*, 2017, **5**, 2488–2503.

4 B. Anasori, M. R. Lukatskaya and Y. Gogotsi, *Nature Reviews Materials*, 2017, **2**,.

5 H. Wang, Y. Wu, X. Yuan, G. Zeng, J. Zhou, X. Wang and J. W. Chew, *Advanced Materials*, 2018, **30**, 1704561.

6 N. K. Chaudhari, H. Jin, B. Kim, D. San Baek, S. H. Joo and K. Lee, *Journal of Materials Chemistry A*, 2017, **5**, 24564–24579.

7 C. Zhang, B. Anasori, A. Seral-Ascaso, S.-H. Park, N. McEvoy, A. Shmeliov, G. S. Duesberg, J. N. Coleman, Y. Gogotsi and V. Nicolosi, *Advanced materials*, 2017, **29**, 1702678.

8 M. Naguib, O. Mashtalir, J. Carle, V. Presser, J. Lu, L. Hultman, Y. Gogotsi and M. W. Barsoum, *ACS nano*, 2012, **6**, 1322–1331.

9 J. L. Hart, K. Hantanasirisakul, A. C. Lang, B. Anasori, D. Pinto, Y. Pivak, J. T. van Omme, S. J. May, Y. Gogotsi and M. L. Taheri, *Nature communications*, 2019, **10**, 1–10.

10 J. Luo, X. Tao, J. Zhang, Y. Xia, H. Huang, L. Zhang, Y. Gan, C. Liang and W. Zhang, *ACS nano*, 2016, **10**, 2491–2499.

11 M. R. Lukatskaya, S. Kota, Z. Lin, M.-Q. Zhao, N. Shpigel, M. D. Levi, J. Halim, P.-L. Taberna, M. W. Barsoum, P. Simon and Y. Gogotsi, *Nature Energy*, 2017, **2**,.

12 Y. A. Al-Hamadani, B.-M. Jun, M. Yoon, N. Taheri-Qazvini, S. A. Snyder, M. Jang, J. Heo and Y. Yoon, *Chemosphere*, 2020, **254**, 126821.

13 T. Liu, X. Liu, N. Graham, W. Yu and K. Sun, *Journal of Membrane Science*, 2020, **593**, 117431.

14 H. Pan, *Scientific reports*, 2016, **6**, 1–10.

15 J. Ran, G. Gao, F.-T. Li, T.-Y. Ma, A. Du and S.-Z. Qiao, *Nature communications*, 2017, **8**, 1–10.

16 G. Gao, A. P. O'Mullane and A. Du, *Acs Catalysis*, 2017, **7**, 494–500.

17 K. Hantanasirisakul, M.-Q. Zhao, P. Urbankowski, J. Halim,

B. Anasori, S. Kota, C. E. Ren, M. W. Barsoum and Y. Gogotsi, *Advanced Electronic Materials*, 2016, **2**, 1600050.

18 A. D. Dillon, M. J. Ghidiu, A. L. Krick, J. Griggs, S. J. May, Y. Gogotsi, M. W. Barsoum and A. T. Fafarman, *Advanced Functional Materials*, 2016, **26**, 4162–4168.

19 G. Ying, A. D. Dillon, A. T. Fafarman and M. W. Barsoum, *Materials Research Letters*, 2017, **5**, 391–398.

20 M. Soleymaniha, M.-A. Shahbazi, A. R. Rafieerad, A. Maleki and A. Amiri, *Advanced healthcare materials*, 2019, **8**, 1801137.

21 K. Huang, Z. Li, J. Lin, G. Han and P. Huang, *Chemical Society Reviews*, 2018, **47**, 5109–5124.

22 R. Li and Y. Wang, *Nature communications*, 2019, **10**, 1–8.

23 A. Sarycheva, A. Polemi, Y. Liu, K. Dandekar, B. Anasori and Y. Gogotsi, *Science advances*, 2018, **4**, eaau0920.

24 P. O. Persson and J. Rosen, *Current Opinion in Solid State and Materials Science*, 2019, **23**, 100774.

25 C. Zhan, W. Sun, Y. Xie, D. en Jiang and P. R. C. Kent, *ACS Applied Materials & Interfaces*, 2019, **11**,.

26 J. Jia, B. Li, S. Duan, Z. Cui and H. Gao, *Nanoscale*, 2019, **11**, 20307–20314.

27 M. Zafari, A. S. Nissimagoudar, M. Umer, G. Lee and K. S. Kim, *Journal of Materials Chemistry A*, 2021, **9**, 9203–9213.

28 X. Yang, C. Shang, S. Zhou and J. Zhao, *Nanoscale Horizons*, 2020, **5**, 1106–1115.

29 M. Khazaei, J. Wang, M. Estili, A. Ranjbar, S. Suehara, M. Arai, K. Esfarjani and S. Yunoki, *Nanoscale*, 2019, **11**, 11305–11314.

30 T. L. Tan, H. M. Jin, M. B. Sullivan, B. Anasori and Y. Gogotsi, *ACS nano*, 2017, **11**, 4407–4418.

31 B. Ahmed, A. E. Ghazaly and J. Rosen, *Advanced Functional Materials*, 2020, **30**, 2000894.

32 Q. Gao and H. Zhang, *Nanoscale*, 2020, **12**, 5995–6001.

33 S. Haastrup, M. Strange, M. Pandey, T. Deilmann, P. S. Schmidt, N. F. Hinsche, M. N. Gjerding, D. Torelli, P. M. Larsen, A. C. Riis-Jensen, J. Gath, K. W. Jacobsen, J. J. Mortensen, T. Olsen and K. S. Thygesen, *2D Materials*, 2018, **5**, 042002.

34 K. Mathew, J. H. Montoya, A. Faghaninia, S. Dwarakanath, M. Aykol, H. Tang, I. heng Chu, T. Smidt, B. Bocklund, M. Horton, J. Dagdelen, B. Wood, Z.-K. Liu, J. Neaton, S. P. Ong, K. Persson and A. Jain, *Computational Materials Science*, 2017, **139**, 140–152.

35 G. Pizzi, A. Cepellotti, R. Sabatini, N. Marzari and B. Kozinsky, *Computational Materials Science*, 2016, **111**, 218–230.

36 A. Jain, S. P. Ong, W. Chen, B. Medasani, X. Qu, M. Kocher, M. Brafman, G. Petretto, G.-M. Rignanese, G. Hautier, D. Gunter and K. A. Persson, *Concurrency and Computation: Practice and Experience*, 2015, **27**, 5037–5059.

37 J.-H. Yang, Y. Zhang, W.-J. Yin, X. Gong, B. I. Yakobson and S.-H. Wei, *Nano letters*, 2016, **16**, 1110–1117.

38 C. Zhang and Q. Sun, *The journal of physical chemistry letters*, 2016, **7**, 2664–2670.

39 V. Skákalová and A. B. Kaiser, *Graphene: properties, preparation, characterisation and devices*, Elsevier, 2014.

40 D. Andrews, G. Scholes and G. Wiederrecht, *Comprehensive nanoscience and technology*, Academic Press, 2010.

41 I. Ozdemir, Y. Kadioglu, O. U. Akturk, Y. Yuksel, U. Akinci and E. Akturk, *Journal of Physics: Condensed Matter*, 2019, **31**, 505401.

42 J. Zhou, J. Palisaitis, J. Halim, M. Dahlqvist, Q. Tao, I. Persson, L. Hultman, P. O. Å. Persson and J. Rosen, *Science*, 2021, **373**, 801–805.

43 J. Zhu, M. Wang, M. Lyu, Y. Jiao, A. Du, B. Luo, I. Gentle and L. Wang, *ACS Applied Nano Materials*, 2018, **1**,.

44 W. Sun, H.-W. Wang, L. Vlcek, J. Peng, A. B. Brady, N. C. Osti, E. Mamontov, M. Tyagi, J. Nanda, S. G. Greenbaum, P. R. C. Kent and M. Naguib, *Advanced Materials Interfaces*, 2020, **7**, 1902207.

45 Z. Du, C. Wu, Y. Chen, Q. Zhu, Y. Cui, H. Wang, Y. Zhang, X. Chen, J. Shang, B. Li, W. Chen, C. Liu and S. Yang, *Advanced Energy Materials*, 2021, 2103228.

46 D. Wang, Z. Sun, D. Han, L. Liu and L. Niu, *RSC Advances*, 2017, **7**, 11834–11839.

47 Y.-Y. Wu, T. Bo, X. Zhu, Z. Wang, J. Wu, Y. Li and B.-T. Wang, *Applied Surface Science*, 2020, **513**, 145821.

48 M. N. Gjerding, A. Taghizadeh, A. Rasmussen, S. Ali, F. Bertoldo, T. Deilmann, N. R. Knøsgaard, M. Kruse, A. H. Larsen, S. Manti, T. G. Pedersen, U. Petralanda, T. Skovhus, M. K. Svendsen, J. J. Mortensen, T. Olsen and K. S. Thygesen, *2D Materials*, 2021, **8**, 044002.

49 J. P. Perdew, K. Burke and M. Ernzerhof, *Physical Review Letters*, 1996, **77**, 3865.

50 J. J. Mortensen, L. B. Hansen and K. W. Jacobsen, *Physical Review B*, 2005, **71**, 035109.

51 J. Heyd, G. E. Scuseria and M. Ernzerhof, *The Journal of chemical physics*, 2003, **118**, 8207–8215.

52 J. Paier, M. Marsman, K. Hummer, G. Kresse, I. C. Gerber and J. G. Ángyán, *The Journal of chemical physics*, 2006, **124**, 154709.

53 M. Gjerding, T. Skovhus, A. Rasmussen, F. Bertoldo, A. H. Larsen, J. J. Mortensen and K. S. Thygesen, *Computational Materials Science*, 2021, **199**, 110731.

54 A. H. Larsen, J. J. Mortensen, J. Blomqvist, I. E. Castelli, R. Christensen, M. Dułak, J. Friis, M. N. Groves, B. Hammer, C. Hargus, E. D. Hermes, P. C. Jennings, P. B. Jensen, J. Kermode, J. R. Kitchin, E. L. Kolsbjerg, J. Kubal, K. Kaasbjerg, S. Lysgaard, J. B. Maronsson, T. Maxson, T. Olsen, L. Pastewka, A. Peterson, C. Rostgaard, J. Schiøtz, O. Schütt, M. Strange, K. S. Thygesen, T. Vegge, L. Vilhelmsen, M. Walter, Z. Zeng and K. W. Jacobsen, *Journal of Physics: Condensed Matter*, 2017, **29**, 273002.

55 G. Kresse and J. Furthmüller, *Physical review B*, 1996, **54**, 11169.

56 Q. Tang, Z. Zhou and P. Shen, *Journal of the American Chemical Society*, 2012, **134**, 16909–16916.

57 C. Eames and M. S. Islam, *Journal of the American Chemical Society*, 2014, **136**, 16270–16276.

58 M. Liu, Z. Rong, R. Malik, P. Canepa, A. Jain, G. Ceder and K. A. Persson, *Energy & Environmental Science*, 2015, **8**, 964–974.

59 O. I. Malyi, K. V. Sopiha and C. Persson, *ACS applied materials & interfaces*, 2019, **11**, 24876–24884.

60 A. Togo and I. Tanaka, *Scripta Materialia*, 2015, **108**, 1–5.

61 K. Gaál-Nagy and D. Strauch, *arXiv preprint arXiv:0707.0384*, 2007, .

62 F. Mouhat and F.-X. Coudert, *Physical review B*, 2014, **90**, 224104.

63 S. Zhang, J. Zhou, Q. Wang, X. Chen, Y. Kawazoe and P. Jena, *Proceedings of the National Academy of Sciences*, 2015, **112**, 2372–2377.

64 T. Hu, J. Yang, W. Li, X. Wang and C. M. Li, *Physical Chemistry Chemical Physics*, 2020, **22**, 2115–2121.

65 O. Mashtalir, K. M. Cook, V. N. Mochalin, M. Crowe, M. W. Barsoum and Y. Gogotsi, *Journal of Materials Chemistry A*, 2014, **2**, 14334–14338.

66 Y. Xie and P. R. C. Kent, *Physical Review B*, 2013, **87**, 235441.

67 N. Zhang, Y. Hong, S. Yazdanparast and M. A. Zaeem, *2D Materials*, 2018, **5**, 045004.

68 G. Ceder, M. Aydinol and A. Kohan, *Computational materials science*, 1997, **8**, 161–169.

69 A. Iqbal, F. Shahzad, K. Hantanasirisakul, M.-K. Kim, J. Kwon, J. Hong, H. Kim, D. Kim, Y. Gogotsi and C. M. Koo, *Science*, 2020, **369**, 446–450.

70 C. Zhi, Y. Bando, C. Tang, H. Kuwahara and D. Golberg, *Advanced Materials*, 2009, **21**, 2889–2893.

71 K. Kang, S. Xie, L. Huang, Y. Han, P. Y. Huang, K. F. Mak, C.-J. Kim, D. Muller and J. Park, *Nature*, 2015, **520**, 656–660.